



CHORUS

This is the accepted manuscript made available via CHORUS. The article has been published as:

Transport of indirect excitons in high magnetic fields

Y. Y. Kuznetsova, C. J. Dorow, E. V. Calman, L. V. Butov, J. Wilkes, E. A. Muljarov, K. L. Campman, and A. C. Gossard

Phys. Rev. B **95**, 125304 — Published 6 March 2017

DOI: [10.1103/PhysRevB.95.125304](https://doi.org/10.1103/PhysRevB.95.125304)

Transport of Indirect Excitons in High Magnetic Fields

Y. Y. Kuznetsova,¹ C. J. Dorow,¹ E. V. Calman,¹ L. V. Butov,¹
J. Wilkes,² E. A. Muljarov,² K. L. Campman,³ and A. C. Gossard³

¹Department of Physics, University of California at San Diego, La Jolla, California 92093-0319, USA

²School of Physics and Astronomy, Cardiff University, Cardiff CF24 3AA, United Kingdom

³Materials Department, University of California at Santa Barbara, Santa Barbara, CA 93106-5050, USA

(Dated: January 31, 2017)

We present spatially- and spectrally-resolved photoluminescence measurements of indirect excitons in high magnetic fields. Long indirect exciton lifetimes give the opportunity to measure magnetoexciton transport by optical imaging. Indirect excitons formed from electrons and holes at zeroth Landau levels ($0_e - 0_h$ indirect magnetoexcitons) travel over large distances and form a ring emission pattern around the excitation spot. In contrast, the spatial profiles of $1_e - 1_h$ and $2_e - 2_h$ indirect magnetoexciton emission closely follow the laser excitation profile. The $0_e - 0_h$ indirect magnetoexciton transport distance reduces with increasing magnetic field. These effects are explained in terms of magnetoexciton energy relaxation and effective mass enhancement.

PACS numbers: 73.63.Hs, 78.67.De

I. INTRODUCTION

Composite bosons in the high magnetic field regime are particles with remarkable properties. In contrast to regular composite particles, their mass is not determined by the sum of the masses of their constituents, but by the effect of the magnetic field¹⁻⁴. Such peculiarity should significantly modify transport of these exotic particles, making them an interesting subject of research. While the realization of cold fermions (electrons) in high magnetic fields has lead to exciting findings, including the integer and fractional quantum Hall effects⁵, the realization of cold bosons in the high magnetic field regime and measurements of their transport is an open challenge.

The high magnetic field regime for (composite) bosons is realized when the cyclotron splitting becomes comparable to the binding energy of the boson constituents. The fulfillment of this condition for atoms requires very high magnetic fields $B \sim 10^6$ Tesla, and studies of cold atoms therefore use synthetic magnetic fields in rotating systems⁶⁻⁸ and optically synthesized magnetic fields⁹.

Excitons are composite bosons, which offer the opportunity to experimentally realize the high magnetic field regime. Due to the small exciton mass and binding energy, the high magnetic field regime for excitons is realized with magnetic fields of a few Tesla, achievable in lab⁴. There are exciting theoretical predictions for cold two-dimensional (2D) neutral exciton and electron-hole (e-h) systems in high magnetic fields. Predicted collective states include a paired Laughlin liquid¹⁰, an excitonic charge-density-wave state¹¹, and a condensate of magnetoexcitons^{12,13}. Predicted transport phenomena include the exciton Hall effect^{14,15}, superfluidity^{15,16}, and localization¹⁷. Excitons also play an important role in the description of a many-body state in bilayer electron systems in high magnetic fields¹⁸.

2D neutral exciton and e-h systems in high magnetic fields were studied experimentally in single quantum wells (QWs), and excitons and deexcitons were observed

in dense e-h magnetoplasmas^{19,20}. However, short exciton lifetimes in the studied single QWs did not allow the achievement of low exciton temperatures while also limiting exciton transport distance before recombination. These obstacles encountered in studies of excitons in single QWs prevented the approach of the problem of transport of cold bosons in the high magnetic field regime.

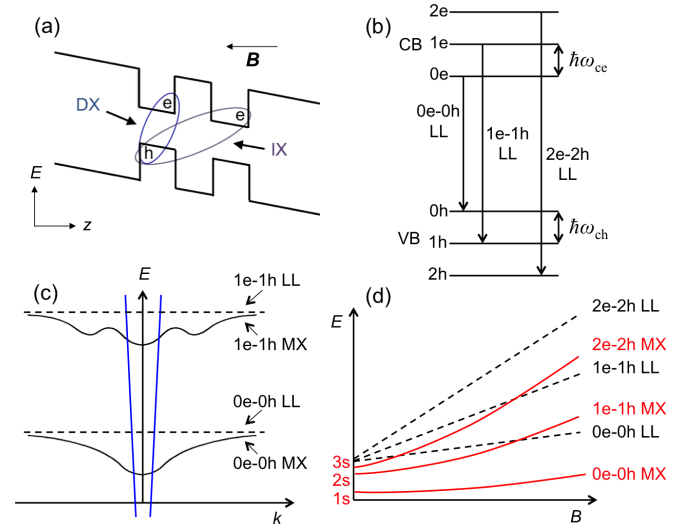


FIG. 1: (a) CQW band diagram. (b) Landau levels (LLs) for electron (e) in conduction band (CB) and hole (h) in valence band (VB). Arrows show allowed optical transitions. (c) Dispersion of magnetoexciton (MX) formed from e and h at zeroth LLs, $0_e - 0_h$, and first LLs, $1_e - 1_h$ (black solid lines). Dashed lines show the sum of the e and h LL energies $1/2\hbar\omega_c$ and $3/2\hbar\omega_c$, respectively. $\omega_c = \omega_{ce} + \omega_{ch}$ is the sum of the electron and hole cyclotron energies. Blue lines show photon dispersion. (d) $k = 0$ exciton energy vs magnetic field B (red solid lines). Dashed black lines show the sum of the e and h LL energies $(N + 1/2)\hbar\omega_c$.

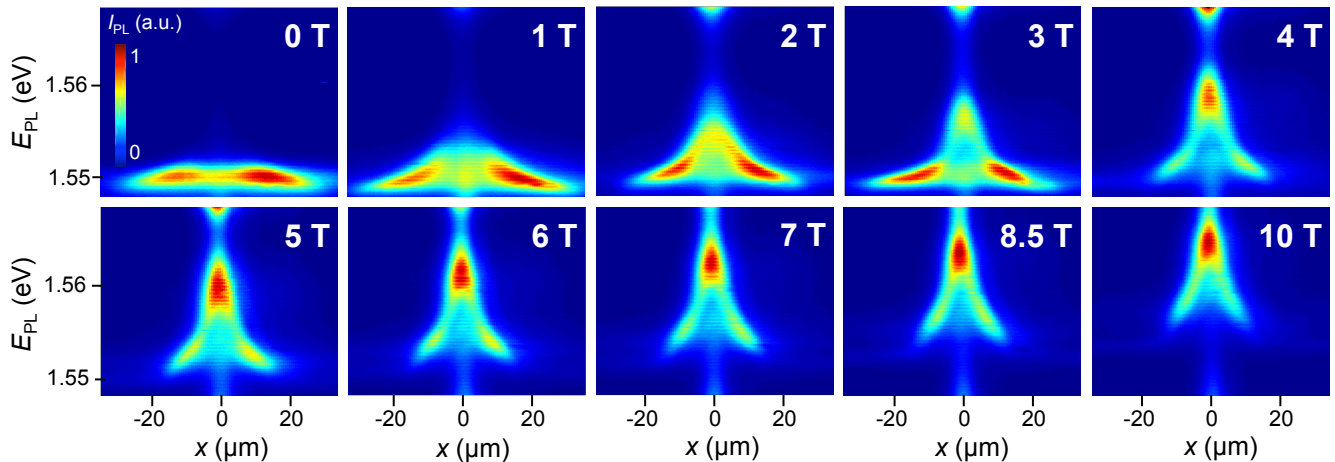


FIG. 2: x -energy IMX emission pattern for $B = 0$ T to 10 T. Excitation power $P_{\text{ex}} = 260 \mu\text{W}$. Laser excitation spot is at $x = 0$.

Here, we present the first measurements of transport of cold bosons in high magnetic fields in a system of indirect excitons. An indirect exciton (IX) is composed of an electron and a hole in spatially separate QW layers and can exist in a coupled QW structure (CQW)^{21,22} [Fig. 1(a)]. Lifetimes of IXs are orders of magnitude longer than lifetimes of regular direct excitons and long enough for the IXs to cool below the temperature of quantum degeneracy $T_0 = 2\pi\hbar^2 n / (gk_B M)^{23}$ (for a GaAs CQW with the exciton spin degeneracy $g = 4$ and mass $M = 0.22m_0$, $T_0 \sim 3$ K for the exciton density per spin state $n/g = 10^{10} \text{ cm}^{-2}$). Furthermore, due to their long lifetimes, IXs can travel over large distances before recombination, allowing the study of exciton transport by optical imaging. Finally, the density of photoexcited e-h systems can be controlled by the laser excitation, which allows the realization of virtually any Landau level filling factor, ranging from fractional $\nu < 1$ to high ν , even at fixed magnetic field. The opportunity to implement low temperatures, the high magnetic field regime, long transport distances, and controllable densities make IXs a model system for studying cold bosons in high magnetic fields. Earlier studies of IXs in magnetic fields addressed IX energies²⁴⁻²⁹, dispersion relations^{4,30-32}, and spin states^{33,34}.

The theory of Mott excitons in high magnetic fields, magnetoexcitons (MXs), was developed in Refs.^{1-4,35,36}. 2D MXs are shown schematically in Fig. 1. Optically active MXs are formed from electrons and holes at Landau levels (LLs) with $N_e = N_h$, where N_e and N_h are the numbers of the LLs of the e and h [Fig. 1(b,c)]. The MX dispersion is determined by the coupling between the MX center-of-mass motion and internal structure: MX is composed of an electron and a hole forced to travel with the same velocity, producing on each other a Coulomb force that is canceled by the Lorentz force. As a result, MXs with momentum k carry an in-plane electric dipole $r_{\text{eh}} = kl_B^2$ in the direction perpendicular

to k , where $l_B = \sqrt{\hbar c / (eB)}$ is the magnetic length. Due to this coupling between the MX center-of-mass motion and internal structure, the MX dispersion can be calculated from the expression of the Coulomb force between the electron and the hole as a function of r_{eh} . At small k , the MX dispersion is parabolic and can be described by an effective MX mass. At high $k \gg 1/l_B$, the separation between electron and hole becomes large, the Coulomb interaction between them vanishes, and the MX energy tends toward the sum of the electron and hole LL energies [Fig. 1(c)]¹⁻⁴. The MX mass and MX binding energy increase with $B^{1-4,15}$. With reducing B , $N_e - N_h$ MX states transform to $(N + 1)s$ exciton states, where $N + 1$ is the principal quantum number [Fig. 1(d)]. These properties are characteristic of both direct MXs (DMXs) and indirect MXs (IMXs). Due to the separation (d) between the e and h layers, IMX energies are lower by $\sim edF_z$ and grow faster with B^{24-30} (F_z is the electric field in the z direction), IMX binding energies are smaller^{4,25,30-32}, and IMX effective masses grow faster with $B^{4,30-32}$.

Free 2D MXs can recombine radiatively when their momentum k is inside the intersection between the dispersion surface $E_{\text{MX}}(k)$ and the photon cone $E = \hbar kc / \sqrt{\epsilon}$, called the radiative zone³⁷⁻³⁹ [Fig. 1(c)]. In GaAs QW structures, the radiative zone corresponds to $k \lesssim k_0 \approx E_g \sqrt{\epsilon} / (\hbar c) \approx 2.7 \times 10^5 \text{ cm}^{-1}$ (ϵ is the dielectric constant, E_g the semiconductor gap). In GaAs QW structures, excitons may have four spin projections on the z direction $J_z = \pm 2, \pm 1$; the $J_z = \pm 1$ states are optically active⁴⁰. Free MXs with $k \lesssim k_0$, $N_e = N_h$, and $J_z = \pm 1$ recombine radiatively directly contributing to MX emission. Free MXs with $k > k_0$, $N_e \neq N_h$, or $J_z = \pm 2$ are dark.

II. II. EXPERIMENT

Experiments were performed on a $n^+ - i - n^+$ GaAs CQW. The i -region consists of a single pair of 8-nm GaAs

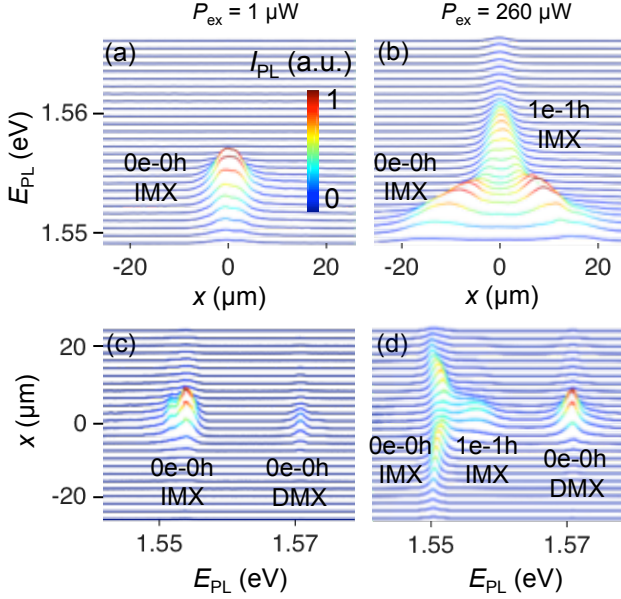


FIG. 3: (a,b) Spatial profiles of the IMX emission at different energies at $P_{\text{ex}} = 1$ (a) and $260 \mu\text{W}$ (b). (c,d) MX spectra at different distances x from the excitation spot center at $P_{\text{ex}} = 1$ (c) and $260 \mu\text{W}$ (d). IMX and DMX lines correspond to indirect and direct MX emission, respectively. The low-energy bulk emission was subtracted from the spectra (Appendix C). The laser excitation profile is shown in Fig. 4(a). $B = 3 \text{ T}$ for all data.

QWs separated by a 4-nm $\text{Al}_{0.33}\text{Ga}_{0.67}\text{As}$ barrier, surrounded by 200-nm $\text{Al}_{0.33}\text{Ga}_{0.67}\text{As}$ layers. The n^+ layers are Si-doped GaAs with Si concentration $5 \times 10^{17} \text{ cm}^{-3}$. The indirect regime, characterized by IX being the lowest energy state, was implemented by applying voltage $V = -1.2 \text{ V}$ between the n^+ layers. The 633 nm cw laser excitation was focused to $\sim 6 \mu\text{m}$ spot. The x -energy images were measured with a liquid-nitrogen-cooled charge-coupled device (CCD) placed after a spectrometer with resolution 0.18 meV. Spatial resolution was $\approx 2.5 \mu\text{m}$. The measurements were performed in an optical dilution refrigerator at temperature $T_{\text{bath}} = 40 \text{ mK}$ and magnetic fields $B = 0 - 10 \text{ T}$ perpendicular to the CQW plane.

Figure 2 shows the evolution of measured x -energy emission patterns with increasing B . Horizontal cross sections of the x -energy emission pattern reveal the spatial profiles at different energies [Fig. 3(a,b)], while vertical cross sections present spectra at different distances x from the excitation spot center [Fig. 3(c,d)]. More spatial profiles and spectra of the IMX emission at different B and P_{ex} are presented in Appendix C. Spatial profiles of the amplitudes of IMX emission lines are shown in Fig. 4(a,b).

The magnetic field dependence [Fig. 4(d)] identifies the $0_e - 0_h$, $1_e - 1_h$, and $2_e - 2_h$ IMX emission lines. The DMX emission is also observed at high energies [Figs. 3, 4(d)].

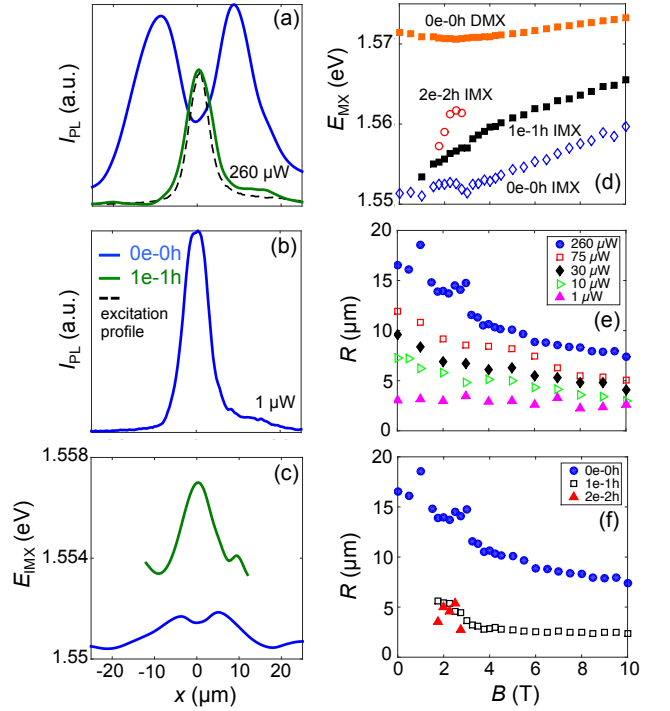


FIG. 4: (a,b) Amplitude of $0_e - 0_h$ and $1_e - 1_h$ IMX emission lines at $P_{\text{ex}} = 260$ (a) and $1 \mu\text{W}$ (b), $B = 3 \text{ T}$. (c) $0_e - 0_h$ and $1_e - 1_h$ IMX energies at $P_{\text{ex}} = 260 \mu\text{W}$, $B = 3 \text{ T}$. (d) IMX energies vs B at $P_{\text{ex}} = 260 \mu\text{W}$. (e) $0_e - 0_h$ IMX emission radius R (half-width-half-maximum) vs B for different P_{ex} . (f) $0_e - 0_h$, $1_e - 1_h$, and $2_e - 2_h$ IMX emission radius vs B for $P_{\text{ex}} = 260 \mu\text{W}$.

At low P_{ex} and, in turn, low IMX densities, the $0_e - 0_h$ IMX emission essentially follows the laser excitation profile [Figs. 3(a,c) and 4(b)]. This indicates that at low densities, $0_e - 0_h$ IMXs are localized in the in-plane disorder potential and practically do not travel beyond the excitation spot. However, at high densities, transport of $0_e - 0_h$ IMXs is observed as the $0_e - 0_h$ IMX emission extends well beyond the excitation spot [Figs. 2, 3(b,d), and 4(a)]. Furthermore, the $0_e - 0_h$ IMX emission shows a ring structure around the excitation spot [Figs. 2, 3(b,d), and 4(a)]. This structure is similar to the inner ring in the IX emission pattern at $B = 0$ ⁴²⁻⁴⁴. The enhancement of $0_e - 0_h$ IMX emission intensity with increasing distance from the center originates from IMX transport and energy relaxation as follows. IMXs cool toward the lattice temperature when they travel away from the laser excitation spot, thus forming a ring of cold IMXs. The cooling increases the occupation of the low-energy optically active IMX states [Fig. 1(c)], producing the $0_e - 0_h$ IMX emission ring. The ring extension R characterizing the $0_e - 0_h$ IMX transport distance is presented in Fig. 4(e,f). The IMX transport distance increases with density [Fig. 4(e,f)]. This effect is explained by the theory presented below in terms of the screening of the structure in-plane disorder by the repulsively interacting IMXs.

In contrast to the $0_e - 0_h$ IMX emission, the spatial

profile of the $1_e - 1_h$ IMX emission closely follows the laser excitation profile [Fig. 4(a)]. The data show that the high-energy $1_e - 1_h$ IMX states are occupied in the excitation spot region (where the IMX temperature and density is maximum). Long range transport is not observed here because the $1_e - 1_h$ IMXs effectively relax in energy and transform to $0_e - 0_h$ IMXs beyond the laser excitation spot where the IMX temperature drops down. $1_e - 1_h$ IMX transport distance within this relaxation time $\lesssim 3 \mu\text{m}$ [Fig. 4(a,f)].

Additionally, the $0_e - 0_h$ and $1_e - 1_h$ IMX energies are observed to reduce with x [Fig. 4(c)]. This energy reduction follows the IMX density reduction away from the excitation spot. The density reduction can lower IX energy due to interactions and localization in the minima of disorder potential. IMXs have a built-in dipole moment $\sim ed$ and interact repulsively. The repulsive IMX interaction causes the reduction of the IMX energy with reducing density. In contrast, direct MXs in single QWs are essentially noninteracting particles and their energy practically does not depend on density^{13,20}.

Figure 4(e,f) also shows that the $0_e - 0_h$ IMX transport distance reduces with B . This effect is explained below in terms of the enhancement of the MX mass. The reduction of the IMX transport distance causes the IMX accumulation in the excitation spot area. The IMX accumulation contributes to the observed enhancement of both the IMX emission intensity and energy in the excitation spot area with increasing B [Fig. 2].

We note also that IX emission patterns may contain the inner ring, which forms due to IX transport and thermalization⁴²⁻⁴⁴, and external ring, which forms on the interface between the hole-rich and electron-rich regions⁴⁵⁻⁴⁹. The data presented in Fig. C1 [Appendix C] show that the external ring and the presence of the charge-rich regions associated with it play no major role in the IMX transport and relaxation phenomena described in this work.

III. THEORY

The following two-body Hamiltonian is used to describe MXs in CQWs under external bias,

$$\hat{H}(\mathbf{r}_e, \mathbf{r}_h) = \hat{H}_e(\mathbf{r}_e) + \hat{H}_h(\mathbf{r}_h) - \frac{e^2}{\epsilon|\mathbf{r}_e - \mathbf{r}_h|} + E_g. \quad (1)$$

Here, $\mathbf{r}_{e(h)}$ and $\hat{H}_{e(h)}$ are the electron (hole) coordinates and single-particle Hamiltonians, respectively. The latter are given by

$$\hat{H}_{e(h)}(\mathbf{r}) = \hat{p}_{e(h)}(\mathbf{r}) \frac{1}{2} \hat{m}_{e(h)}^{-1}(z) \hat{p}_{e(h)}(\mathbf{r}) + U_{e(h)}(z). \quad (2)$$

The magnetic field B contributes to the momentum operators $\hat{p}_{e(h)}(\mathbf{r}) = -i\hbar\nabla_{\mathbf{r}} \pm (e/c)\mathbf{A}(\mathbf{r})$ via the magnetic vector potential \mathbf{A} . The mass tensor $\hat{m}_{e(h)}(z)$ contains the electron (hole) effective masses which are step functions

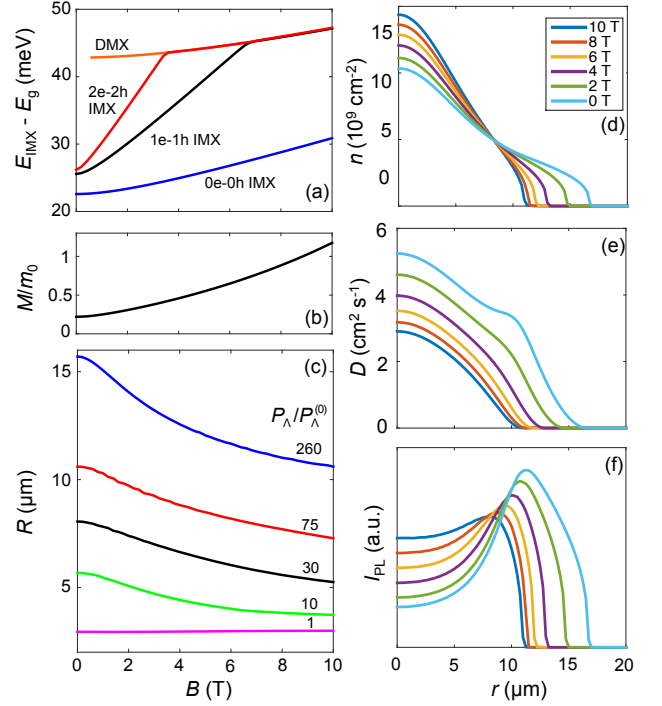


FIG. 5: (a) Optical transition energies of $k = 0$ single MX states measured from the band gap vs B calculated using a multi-sub-level approach. (b) $0_e - 0_h$ IMX mass renormalization due to the magnetic field calculated via perturbation theory. (c) Simulated ring radius R , defined as HWHM of I_{PL} shown in (f), vs B for different injection rates, $P_\Lambda = 2\pi \int_0^\infty \Lambda(r)r dr$ with $P_\Lambda^{(0)} = 0.58 \text{ ns}^{-1}$. Spatial profiles of the (d) density, (e) diffusion coefficient and (f) emission intensity of $0_e - 0_h$ IMX from solving Eqns. (3)-(4) for different B with injection rate $P_\Lambda = 260P_\Lambda^{(0)}$ and $T_{\text{bath}} = 0.5 \text{ K}$.

along z due to the electron and hole confinement in the corresponding QW layers [Fig. 1(a)]. $U_{e(h)}(z)$ contain the QW confinement and the potential due to the applied electric field. The third term in Eq. 1 is the e-h Coulomb interaction. After a factorization of the wave function to separate the center of mass and relative coordinates³⁰, eigen states of the Hamiltonian describing the relative motion of an exciton with $k = 0$ are found using a multi-sub-level approach^{32,50}. This allows the extraction of the B -field dependence of the $k = 0$ IMX energy, E_{IMX} , and radiative lifetime, τ_R . Treating k as a perturbation, we then use perturbation theory to second order to determine the exciton in-plane effective mass enhancement due to the magnetic field, $M(B)$. The calculated E_{IMX} and $M(B)$ are in agreement with the measured E_{IMX} [compare Fig. 5(a) and 4(d)] and $M(B)$ [compare Fig. 5(b) and $M(B)$ in Ref. 4,31].

The B -dependence of the ring in the IMX emission pattern is simulated by combining the microscopic description of a single IMX with a model of IMX transport and thermalization. The following set of coupled equations were solved for the $0_e - 0_h$ IMX density $n(r, t)$ and

temperature $T(r, t)$ in the space-time (r, t) domain,

$$\frac{\partial n}{\partial t} = \nabla [D\nabla n + \mu_x n \nabla(u_0 n)] + \Lambda - \frac{n}{\tau}, \quad (3)$$

$$\frac{\partial T}{\partial t} = S_{\text{pump}} - S_{\text{phonon}}. \quad (4)$$

The two terms in square brackets in the transport equation (3) describe IMX diffusion and drift currents. The latter originates from the repulsive dipolar interactions approximated by $u_0 = 4\pi e^2 d/\epsilon$ within the model⁴³. The diffusion coefficient D and mobility μ_x are related by a generalized Einstein relation, $\mu_x = D(e^{T_0/T} - 1)/(k_B T_0)$. An expression for D is derived using a thermionic model to account for the screening of the random QW disorder potential by dipolar excitons⁴²⁻⁴⁴. D is inversely proportional to the exciton mass M . The enhancement of M with B describes the magnetic field induced reduction in exciton transport. The last two terms on the RHS of (3) describe creation and decay of excitons. $\Lambda(r)$ has a Gaussian profile chosen to match the excitation beam. The optical lifetime τ is the product of τ_R and a factor that accounts for the fraction of excitons that are inside the radiative zone. The effects of IMX in higher levels are included via Λ , since they relax to the $0_e - 0_h$ level within the excitation region.

The thermalization equation (4) describes the balance between heating of excitons by non-resonant photoexcitation and cooling via interaction with bulk longitudinal acoustic phonons. Both rates are modified by the magnetic field due to their dependence on $M(B)$. The emission intensity is extracted from n/τ . In the simulations, $T_{\text{bath}} = 0.5\text{ K}$ was used to avoid the excessive computation times incurred by the dense grids needed to handle the strongly non-linear terms in (3)-(4) that are most prominent at low T . In the temperature range $T_{\text{bath}} = 0.5\text{ K} - 1\text{ K}$, the results of the model are qualitatively similar with the ring radius only slowly varying with T . Modifying the computations for lower T_{bath} forms the subject of future work. Details of the transport and thermalization model including parameters and expressions for D , τ , S_{pump} and S_{phonon} can be found in Appendix A and B.

The simulations show the ring in the IMX emission pattern [Fig. 5(f)] in agreement with the experiment [Fig. 2, 3(b,d), 4(a)]. The increase of the IMX mass causes the reduction of the IMX diffusion coefficient [Fig. 5(e)], contributing to the reduction of the IMX transport distance with magnetic field [Fig. 5(c)]. The measured and simulated reduction of the IMX transport distance with magnetic field are in agreement [compare Fig. 4(e) and 5(c)].

IV. IV. SUMMARY

We measured transport of cold bosons in high magnetic fields in a system of indirect excitons. Indirect magnetoexcitons were observed to be localized at low

exciton densities and delocalized at high exciton densities. Ring and bell-like emission patterns were observed for indirect magnetoexcitons at different Landau levels as well as a reduction of the indirect magnetoexciton transport distance with magnetic field.

V. ACKNOWLEDGMENTS

This work was supported by NSF Grant No. 1407277. J.W. was supported by the EPSRC (grant EP/L022990/1). C.J.D. was supported by the NSF Graduate Research Fellowship Program under Grant No. DGE-1144086.

VI. APPENDIX A: MICROSCOPIC MODEL OF INDIRECT EXCITONS

Optically active eigen states of the exciton Hamiltonian have zero angular momentum and their wave functions, $\Psi(\mathbf{r}_e, \mathbf{r}_h)$, are found by first separating the in-plane center of mass and relative coordinates (\mathbf{R} and ρ , respectively) using the substitution³⁰

$$\Psi_s(\mathbf{r}_e, \mathbf{r}_h) = \psi_{\mathbf{P}}(\rho, \mathbf{R}) \phi_s(\rho, z_e, z_h), \quad (A1)$$

$$\psi_{\mathbf{P}}(\rho, \mathbf{R}) = \exp\left(i\left[\mathbf{P} + \frac{e}{c}\mathbf{A}(\rho)\right] \cdot \frac{\mathbf{R}}{\hbar}\right). \quad (A2)$$

Here, the index s labels the exciton quantized states and \mathbf{P} is the in-plane center-of-mass momentum. We use a cylindrical coordinate system (ρ, z) with $z_{e(h)}$ being the electron (hole) coordinates in the QW growth direction. For a magnetic field $\mathbf{B} = B\hat{z}$ along z , one can use the symmetric gauge for the vector potential $\mathbf{A}(\mathbf{r}) = \frac{1}{2}\mathbf{B} \times \mathbf{r}$. The wave functions $\phi_s(\rho, z_e, z_h)$ describe the internal structure of the exciton and are eigen states of the Hamiltonian,

$$\hat{H}_0(\rho, z_e, z_h) = -\frac{\hbar^2}{2\mu} \left[\frac{\partial^2}{\partial \rho^2} + \frac{1}{\rho} \frac{\partial}{\partial \rho} \right] + \frac{e^2 B^2 \rho^2}{8\mu c^2} - \frac{e^2}{\epsilon \sqrt{\rho^2 + (z_e - z_h)^2}} + \hat{H}_e^{\perp}(z_e) + \hat{H}_h^{\perp}(z_h) + E_g. \quad (A3)$$

The first term on the RHS of (A3) is the kinetic operator of the e-h relative motion with $\rho = |\rho|$ being the radial coordinate in the QW plane and $1/\mu = 1/m_e^{\parallel} + 1/m_h^{\parallel}$ being the exciton in-plane reduced mass. We neglect any z -dependence of the in-plane component of the electron (hole) mass $m_{e(h)}^{\parallel}$ which is justified by low mass contrast in the structure considered here and a minor contribution of the electron and hole wave functions outside the well regions. The second and third terms on the RHS of (A3) are the potentials due to the magnetic field and the electron-hole Coulomb interaction, respectively. E_g is the semiconductor band gap energy. $\phi_s(\rho, z_e, z_h)$ are calculated using a multi-sub-level approach³². This entails

expanding the wave function into the basis of Coulomb-uncorrelated electron-hole pair states,

$$\phi_s(\rho, z_e, z_h) = \sum_l \Phi_l(z_e, z_h) \varphi_l^{(s)}(\rho). \quad (\text{A4})$$

Each pair state, $\Phi_l(z_e, z_h)$, is the product of single particle electron and hole wave functions which themselves are eigen states of the perpendicular motion Hamiltonians,

$$\hat{H}_{e(h)}^\perp(z) = -\frac{\hbar^2}{2} \frac{\partial}{\partial z} \frac{1}{m_{e(h)}^\perp(z)} \frac{\partial}{\partial z} + U_{e(h)}(z), \quad (\text{A5})$$

where $m_{e(h)}^\perp(z)$ is the perpendicular component of the electron (hole) mass. For the ground state exciton, we calculate the transition energy E_x and radial components of the wave functions $\varphi_l^{(s)}(\rho)$ using a matrix generalization of the shooting method with Numerov's algorithm incorporated in the finite difference scheme. From the full solution (A4), we extract the IMX radiative lifetime from the overlap of the electron and hole wave functions, given as

$$\frac{1}{\tau_R} = \frac{2\pi e^2 |d_{cv}|^2 E_x}{\hbar c \sqrt{\varepsilon}} \left| \sum_l \varphi_l^{(0)}(0) \int \Phi_l(z, z) dz \right|^2. \quad (\text{A6})$$

In addition, we find the exciton dipole moment $|\langle z_e - z_h \rangle|$. For high electric fields considered here, the dipole moment is almost constant and we use $d = 11.5$ nm that was measured experimentally from the gradient of the red shift of the indirect exciton energy with respect to electric field²⁶.

To calculate the exciton effective mass enhancement due to the magnetic field, we treat \mathbf{P} as a small parameter and use perturbation theory up to 2nd order. Neglecting non-parabolicity of the exciton band, we find the correction to the exciton energy proportional to $|\mathbf{P}|^2$ and for state s , the renormalized effective mass M_s is given by

$$\frac{1}{M_s} = \frac{1}{M_x} + 2 \left(\frac{2e}{M_x c |\mathbf{p}|} \right)^2 \sum_{m=\pm 1} \frac{|\langle s, 0 | \mathbf{P} \cdot \mathbf{A}(\rho) | j, m \rangle|^2}{E_s - E_j^{(m)}}. \quad (\text{A7})$$

Here, M_x is the exciton mass in the absence of magnetic field. The state $|j, m\rangle$ with magnetic quantum number $m = \pm 1$ and energy $E_j^{(m)}$ is the eigen state of the Hamiltonian that is modified to include angular momentum,

$$\hat{H}_m = \hat{H}_0 + \frac{\hbar^2 m^2}{2\mu \rho^2} + \frac{e\hbar m B}{2\mu c}. \quad (\text{A8})$$

Here $1/\mu = 1/m_e^\parallel - 1/m_h^\parallel$ is the magnetic dipole mass. The summation on the RHS of (A7) converges rapidly and, for the exciton ground state ($s = 0$), about 30 terms are needed to achieve high accuracy. We define $M(B) = M_0(B)$ as the mass of the exciton ground (IMX) state.

VII. APPENDIX B: TRANSPORT AND THERMALIZATION MODEL OF THE EXCITON INNER RING

A thermionic model to account for the transport of excitons in a random QW disorder potential gives the exciton diffusion coefficient, used in Eqn. (3) in the main text, as

$$D = D_0 \frac{M_x}{M(B)} \exp\left(\frac{-U_0}{u_0 n + k_B T}\right). \quad (\text{B1})$$

Here $U_0/2$ is the amplitude of the disorder potential and D_0 is the diffusion coefficient in the absence of disorder with $B = 0$. This model describes effective screening of the disorder potential by repulsively interacting dipolar excitons.

The cooling rate of a quasi-equilibrium exciton gas by interaction with a bath of bulk LA-phonons is

$$S_{\text{phonon}} = \frac{2\pi T^2}{\tau_{\text{sc}} T_0} (1 - e^{-T_0/T}) \times \int_1^\infty \varepsilon \sqrt{\frac{\varepsilon}{\varepsilon - 1} \frac{|F(a \sqrt{\varepsilon(\varepsilon - 1)})|^2}{e^{\varepsilon E_0/k_B T_{\text{bath}}} - 1} \frac{e^{\varepsilon E_0/k_B T} - e^{\varepsilon E_0/k_B T_{\text{bath}}}}{(e^{\varepsilon E_0/k_B T} + e^{-T_0/T} - 1)}} d\varepsilon, \quad (\text{B2})$$

where $\tau_{\text{sc}} = (\pi^2 \hbar^4 \rho_c) / (D_{\text{dp}}^2 M^3(B) v_{\text{LA}})$ is the characteristic exciton-phonon scattering time and $E_0 = 2M(B)v_{\text{LA}}^2$ is the intersection of the exciton and LA-phonon dispersions. ρ_c is the crystal density, D_{dp} is the deformation potential of the exciton—LA-phonon interaction and v_{LA} is the sound velocity. The form factor F originates from an infinite rectangular QW confinement potential for the exciton and is given by

$$F(x) = \frac{\sin(x)}{x} \frac{e^{ix}}{1 - (x/\pi)^2}, \quad (\text{B3})$$

and $a = d_{\text{QW}} M(B) v_{\text{LA}} / \hbar$ is a dimensionless constant with d_{QW} being the QW thickness.

The heating rate due to injection of high energy excitons by non-resonant laser excitation is given by

$$S_{\text{pump}} = \frac{E_{\text{inc}} - k_B T I_2}{2k_B T I_1 - k_B T_0 I_2} \left(\frac{\pi \hbar^2}{2k_B M(B)} \right) \Lambda(r) \quad (\text{B4})$$

where E_{inc} is the excess energy of incoming excitons. The integrals $I_{1(2)}(T_0/T)$ are

$$I_1 = (1 - e^{-T_0/T}) \int_0^\infty \frac{z}{e^z + e^{-T_0/T} - 1} dz, \quad (\text{B5})$$

$$I_2 = e^{-T_0/T} \int_0^\infty \frac{z e^z}{(e^z + e^{-T_0/T} - 1)^2} dz. \quad (\text{B6})$$

Finally, the optical decay rate of excitons is given by

$$\Gamma(z_0) = \frac{1}{\tau_R(B)} \left(\frac{E_\gamma}{2k_B T_0} \right) \times \int_{z_0}^1 \frac{1 + z^2}{[(e^{E_\gamma/k_B T}) / (1 - e^{-T_0/T})] e^{-z^2 E_\gamma/k_B T} - 1} dz. \quad (\text{B7})$$

TABLE I: Parameters of the model

ϵ	Relative permittivity	12.1
E_g	GaAs band gap	1.519 eV
$m_e^\pm(z)$	Electron mass in QW	$0.0665 m_0$
	Electron mass in barrier	$0.0941 m_0$
$m_h^\pm(z)$	Hole mass in QW	$0.34 m_0$
	Hole mass in barrier	$0.48 m_0$
M_x	In-plane exciton mass	$0.22 m_0$
μ	In-plane reduced exciton mass	$0.049 m_0$
κ	Exciton magnetic dipole mass	$0.11 m_0$
d_{co}	Dipole matrix element	0.6 nm
F_z	Applied electric field	21.8 kV/cm
E_{inc}	Energy of incoming excitons	12.9 meV
d	IMX dipole length	11.5 nm
D_{dp}	Deformation potential	8.8 eV
d_{QW}	QW width	8 nm
D_0	Diffusion coefficient without disorder	$30 \text{ cm}^2/\text{s}$
α	Aperture angle of the CCD	30°
ρ_c	Crystal density of GaAs	5.3 g/cm^3
v_{LA}	Sound velocity in GaAs	$3.7 \times 10^5 \text{ cm/s}$
U_0	Amplitude of the disorder potential	2 meV

The energy E_γ marks the exciton energy $(\hbar^2 k^2)/(2M(B))$ at the intersection of the exciton dispersion and the photon dispersion. We find the optical lifetime $\tau = 1/\Gamma(z_0 = 0)$ and photoluminescence intensity $I_{PL} = \Gamma(z_0 = 1 - \sin^2(\alpha/2))n$. In the latter, the lower limit of integration takes into account the finite aperture angle of the CCD, α .

In the transport and thermalization model outlined here, the dependence on magnetic field enters via $M(B)$, $E_x(B)$ and $\tau_R(B)$ as explicitly indicated. It also enters the model via the quantum degeneracy temperature T_0 which is inversely proportional to $M(B)$ (see main text). Table I lists the parameters used.

VIII. APPENDIX C: ANALYSIS AND DATA

IX emission patterns may contain the inner ring, which forms due to IX transport and thermalization⁴²⁻⁴⁴, and external ring, which forms on the interface between the hole-rich and electron-rich regions⁴⁵⁻⁴⁹. For all P_{ex} studied here, the external ring is not observed at $B = 0$. It is observed in magnetic fields for the two highest studied excitation powers, at $B \gtrsim B_{\text{ext-ring}} \sim 3 \text{ T}$ for $P_{ex} = 260 \mu\text{W}$ and at $B \gtrsim B_{\text{ext-ring}} \sim 6 \text{ T}$ for $P_{ex} = 75 \mu\text{W}$ [Fig. C1].

For low studied $P_{ex} < 75 \mu\text{W}$ and for the high $P_{ex} = 75$ and $260 \mu\text{W}$ at $B < B_{\text{ext-ring}}$, the external ring is not observed (its radius is smaller than the inner ring radius), so the inner ring is beyond the hole-rich region. In contrast, for $P_{ex} = 75$ and $260 \mu\text{W}$ and $B > B_{\text{ext-ring}}$, the external ring forms [Fig. C1] and the inner ring is within

the hole-rich region. However, in both these regimes, all observed phenomena, including the inner ring in $0_e - 0_h$ IMX emission beyond the laser excitation spot, bell-like pattern of the $1_e - 1_h$ IMX emission closely following the laser excitation spot, and the reduction of the $0_e - 0_h$ IMX transport distance with increasing magnetic field, are essentially the same. This indicates that the external ring as well as the presence of the hole-rich region associated with it play no major role in the IMX transport and relaxation phenomena described in this work. An effect of the external ring can be seen in an increase of the apparent inner ring radius when the external ring passes through the inner ring, such increase is observed e.g. for $P_{ex} = 260 \mu\text{W}$ around $B = 3 \text{ T}$ [Fig. C1(d)].

Spatial profiles and spectra of the IMX emission at different B and P_{ex} are presented in Figs. C2 and C3. Emission of bulk n^+ -GaAs layers is observed at low energies. The profiles of bulk, $0_e - 0_h$, and $1_e - 1_h$ emission lines were separated as shown in Fig. C4. The bulk emission is subtracted from the spectra presented in Fig. 3 in the main text. The amplitudes, energies, and spatial extensions of the $0_e - 0_h$ and $1_e - 1_h$ IMX emission lines are presented in Fig. 4 in the main text. Figure C5 shows amplitude of emission intensity of $0_e - 0_h$ and $1_e - 1_h$ IMXs for several B .

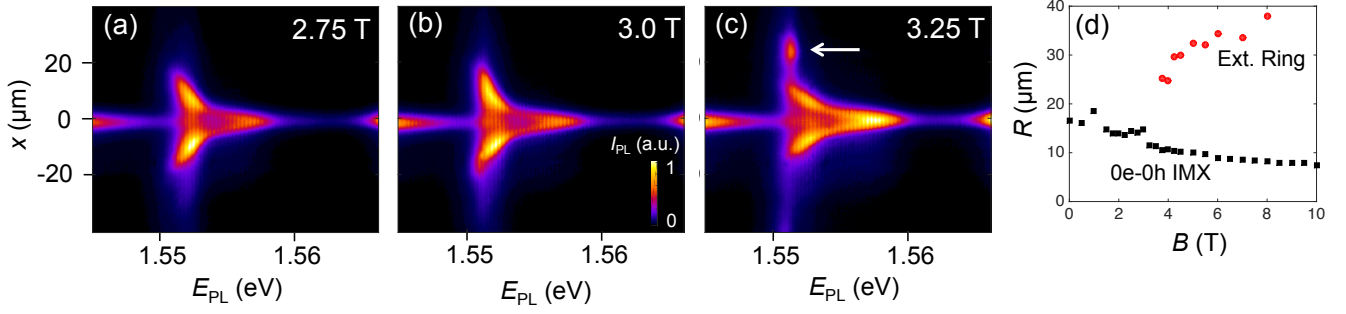


FIG. C1: (a-c) IMX emission for several B at $P_{\text{ex}} = 260 \mu\text{W}$. The external ring is visible in (c). It is indicated by white arrow. (d) Radius of the external ring (red circles) and inner ring (black squares) for $0_e - 0_h$ IMX emission as a function of B . Enlargement of the $0_e - 0_h$ inner ring apparent radius is observed where external ring passes through at $B \sim 3$ T. $P_{\text{ex}} = 260 \mu\text{W}$.

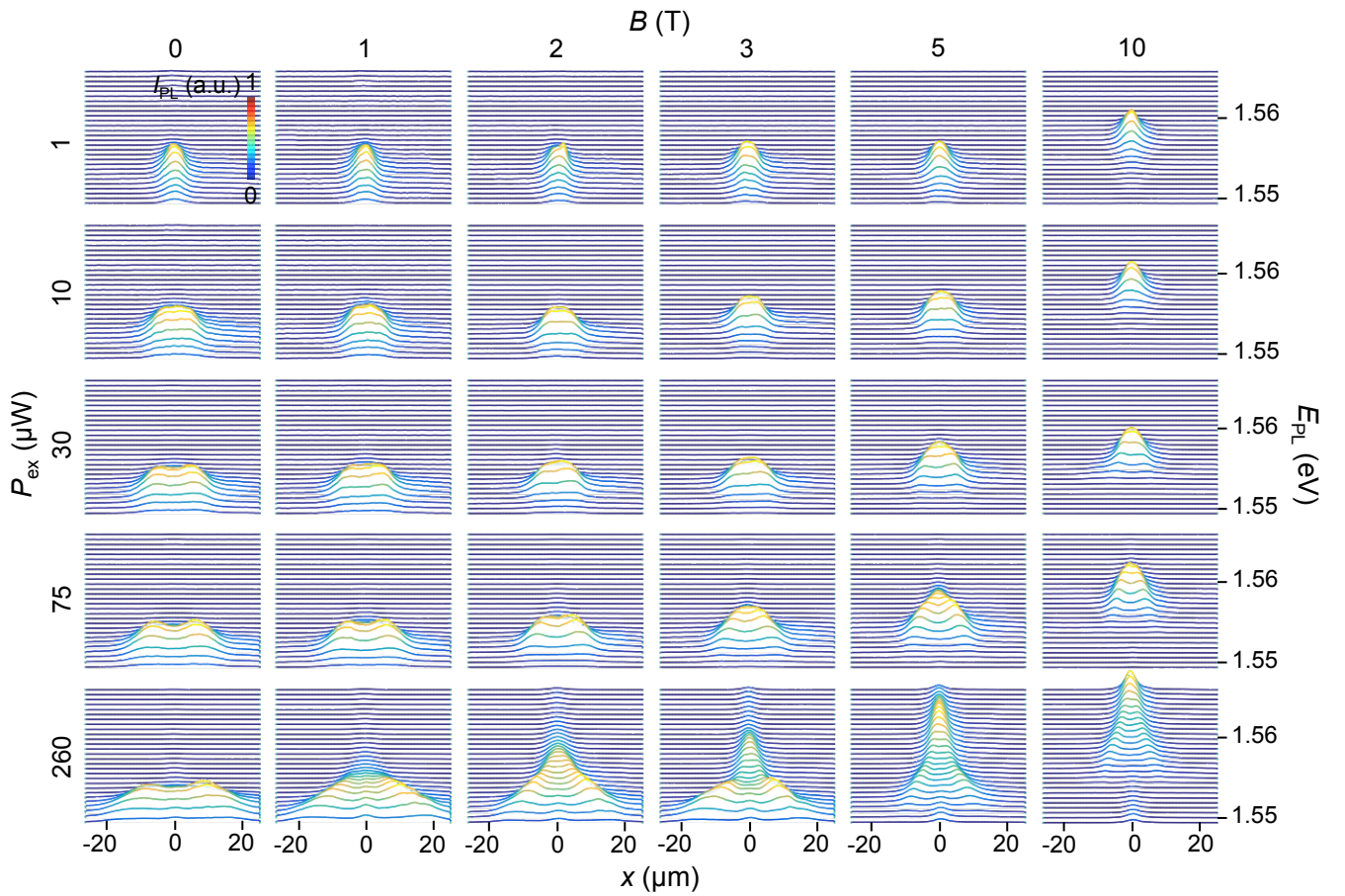


FIG. C2: Horizontal cross sections of x -energy IMX emission pattern for several B and P_{ex} . Spatial profiles at different energies are revealed. Laser excitation profile is shown in Fig. C5.

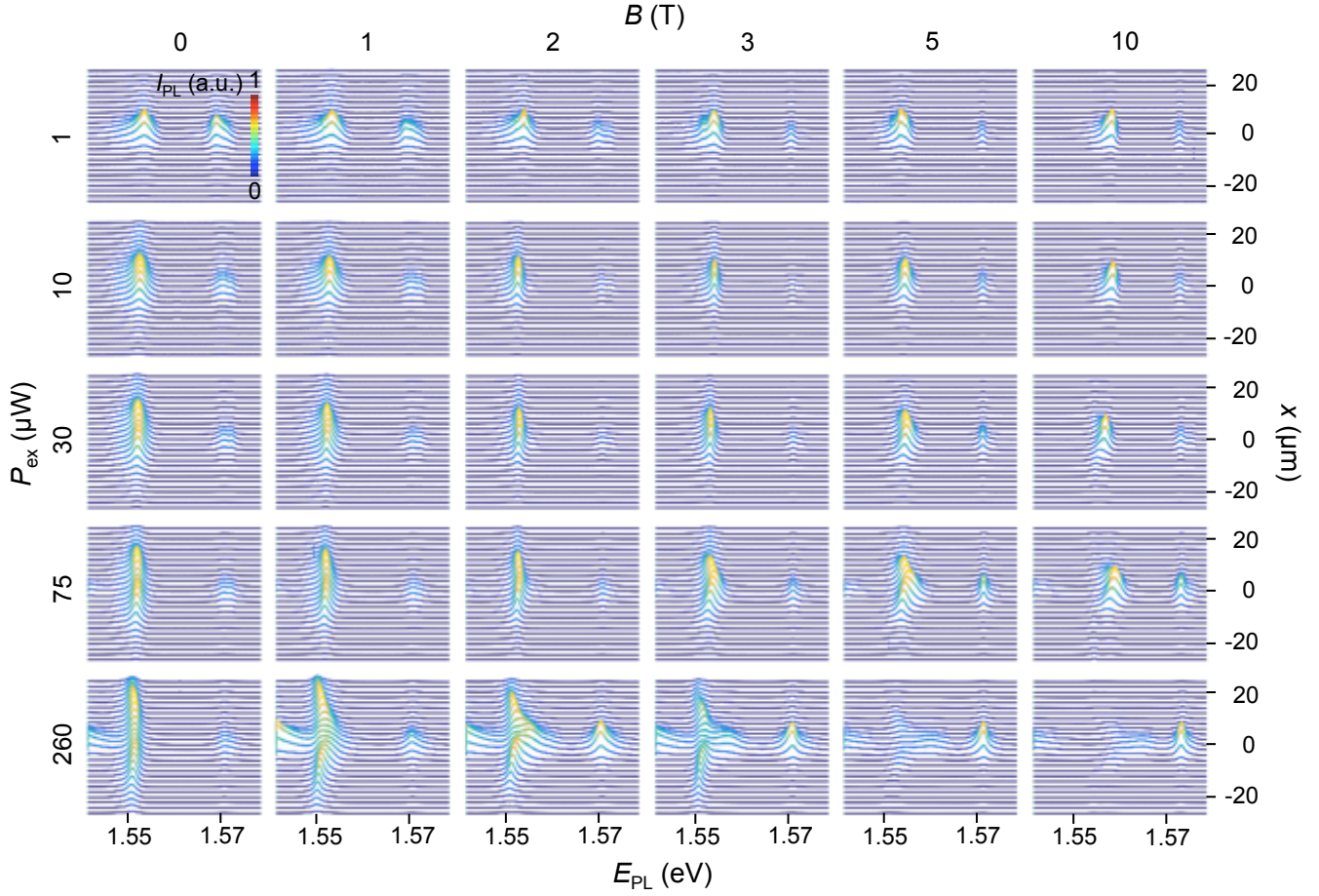


FIG. C3: Vertical cross sections of x -energy IMX emission pattern for several B and P_{ex} . Spectra at different distances from the excitation spot are revealed. Laser excitation profile is shown in Fig. C5.

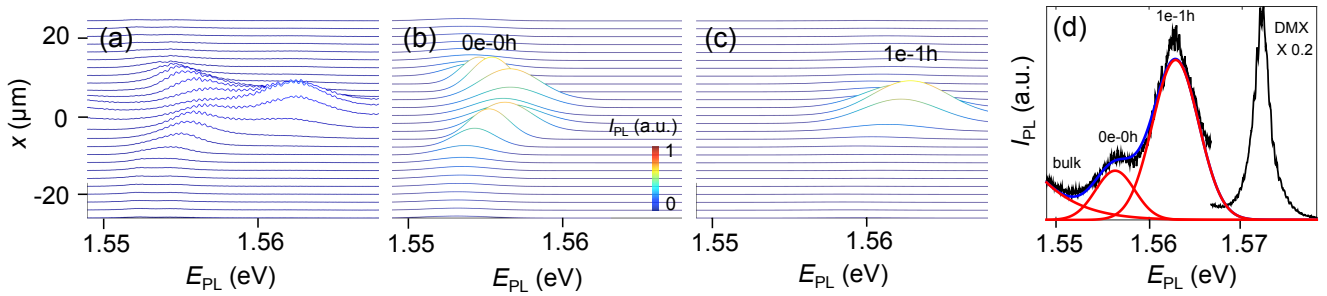


FIG. C4: Summary of fits of IMX lines and low-energy bulk emission. (a) Spectral cuts of raw data. Gaussian fits of the $0_e - 0_h$ (b) and $1_e - 1_h$ (c) IMX spectra. (d) Individual (red) and sum (blue) of the IMX lines and bulk emission compared to raw data (black) at $x = 0$. For all data $P_{\text{ex}} = 260 \mu\text{W}$, $B = 7 \text{ T}$.

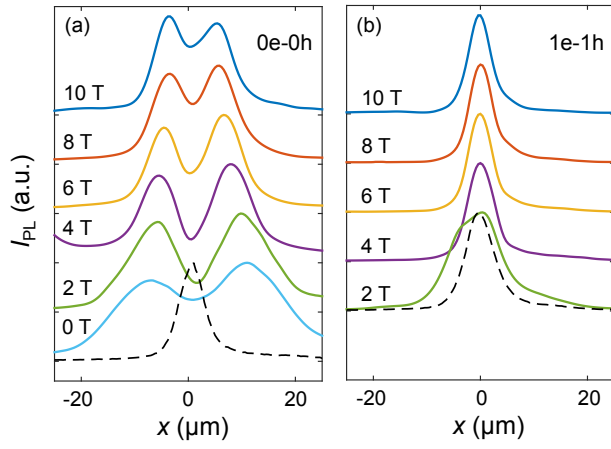


FIG. C5: Amplitude of emission intensity of $0_e - 0_h$ (a) and $1_e - 1_h$ (b) IMXs for several B . Dashed line shows laser excitation profile. $P_{\text{ex}} = 260 \mu\text{W}$ for all data.

- ¹ L.P. Gorkov, I.E. Dzyaloshinskii, Sov. Phys. JETP **26**, 449 (1968).
- ² I.V. Lerner, Yu. E. Lozovik, Sov. Phys. JETP **51**, 588 (1980).
- ³ C. Kallin, B.I. Halperin, Phys. Rev. B **30**, 5655 (1984).
- ⁴ Yu.E. Lozovik, I.V. Ovchinnikov, S.Yu. Volkov, L.V. Butov, D.S. Chemla, Phys. Rev. B **65**, 235304 (2002).
- ⁵ For reviews, see *Perspectives in Quantum Hall Effects*, Ed. S. Das Sarma, A. Pinczuk (Wiley, New York, 1997); H.L. Störmer, D.C. Tsui, A.C. Gossard, Rev. Mod. Phys. **71**, S298 (1999).
- ⁶ K.W. Madison, F. Chevy, W. Wohlleben, J. Dalibard, Phys. Rev. Lett. **84**, 806 (2000).
- ⁷ J.R. Abo-Shaeer, C. Raman, J.M. Vogels, W. Ketterle, Science **292**, 476 (2001).
- ⁸ V. Schweikhard, I. Coddington, P. Engels, V.P. Mogendorff, E.A. Cornell, Phys. Rev. Lett. **92**, 040404 (2004).
- ⁹ Y.-J. Lin, R.L. Compton, K. Jiménez-García, J.V. Porto, I.B. Spielman, Nature **462**, 628 (2009).
- ¹⁰ D. Yoshioka, A.H. MacDonald, J. Phys. Soc. Jpn. **59**, 4211 (1990).
- ¹¹ X.M. Chen, J.J. Quinn, Phys. Rev. Lett. **67**, 895 (1991).
- ¹² Y. Kuramoto, C. Horie, Solid State Commun. **25**, 713 (1978).
- ¹³ I.V. Lerner, Yu.E. Lozovik, Sov. Phys. JETP **53**, 763 (1981).
- ¹⁴ A.B. Dzyubenko, Yu.E. Lozovik, Sov. Phys. Solid State **26**, 938 (1984).
- ¹⁵ D. Paquet, T.M. Rice, K. Ueda, Phys. Rev. B **32**, 5208 (1985).
- ¹⁶ A. Imamoglu, Phys. Rev. B **54**, R14285 (1996).
- ¹⁷ P.I. Arseyev, A.B. Dzyubenko, Phys. Rev. B **52**, R2261 (1995).
- ¹⁸ J.P. Eisenstein, A.H. MacDonald, Nature **432**, 691 (2004).
- ¹⁹ L.V. Butov, V.D. Kulakovskii, E.I. Rashba, Sov. Phys. JETP Lett. **53**, 109 (1991).
- ²⁰ L.V. Butov, V.D. Kulakovskii, G.E.W. Bauer, A. Forchel, D. Grützmacher, Phys. Rev. B **46**, 12765 (1992).
- ²¹ Yu.E. Lozovik, V.I. Yudson, Sov. Phys. JETP **44**, 389 (1976).
- ²² T. Fukuzawa, S. Kano, T. Gustafson, T. Ogawa, Surf. Sci. **228**, 482 (1990).
- ²³ L.V. Butov, A.L. Ivanov, A. Imamoglu, P.B. Littlewood, A.A. Shashkin, V.T. Dolgoplov, K.L. Campman, A.C. Gossard, Phys. Rev. Lett. **86**, 5608 (2001).
- ²⁴ L.V. Butov, A. Zrenner, G. Abstreiter, A.V. Petinova, K. Eberl, Phys. Rev. B **52**, 12153 (1995).
- ²⁵ A.B. Dzyubenko, A.L. Yablonski, Phys. Rev. B **53**, 16355 (1996).
- ²⁶ L.V. Butov, A.A. Shashkin, V.T. Dolgoplov, K.L. Campman, A.C. Gossard, Phys. Rev. B **60**, 8753 (1999).
- ²⁷ L.V. Butov, A. Imamoglu, K.L. Campman, A.C. Gossard, J. Exp. Theor. Phys. **92**, 260 (2001).
- ²⁸ K. Kowalik-Seidl, X.P. Vögele, F. Seilmeier, D. Schuh, W. Wegscheider, A.W. Holleitner, J.P. Kotthaus, Phys. Rev. B **83**, 081307(R) (2011).
- ²⁹ G.J. Schinner, J. Repp, K. Kowalik-Seidl, E. Schubert, M.P. Stalhofer, A.K. Rai, D. Reuter, A.D. Wieck, A.O. Govorov, A.W. Holleitner, J.P. Kotthaus, Phys. Rev. B **87**, 041303(R) (2013).
- ³⁰ Yu.E. Lozovik, A.M. Ruvinskii, Sov. Phys. JETP **85**, 979 (1997).
- ³¹ L.V. Butov, C.W. Lai, D.S. Chemla, Yu.E. Lozovik, K.L. Campman, A.C. Gossard, Phys. Rev. Lett. **87**, 216804 (2001).
- ³² J. Wilkes, E.A. Muljarov, New J. Phys. **18**, 023032 (2016).
- ³³ A.V. Gorbunov, V.B. Timofeev, Solid State Commun. **157**, 6 (2013).
- ³⁴ A.A. High, A.T. Hammack, J.R. Leonard, Sen Yang, L.V. Butov, T. Ostatnický, M. Vladimirova, A.V. Kavokin, T.C.H. Liew, K.L. Campman, A.C. Gossard, Phys. Rev. Lett. **110**, 246403 (2013).
- ³⁵ R.J. Elliott, R. Loudon, J. Phys. Chem. Solids **8**, 382 (1959); **15**, 196 (1960).
- ³⁶ H. Hasegawa, R.E. Howard, J. Phys. Chem. Solids **21**, 179 (1961).
- ³⁷ J. Feldmann, G. Peter, E.O. Göbel, P. Dawson, K. Moore, C. Foxon, R.J. Elliott, Phys. Rev. Lett. **59**, 2337 (1987).
- ³⁸ E. Hanamura, Phys. Rev. B **38**, 1228 (1988).
- ³⁹ L.C. Andreani, F. Tassone, F. Bassani, Solid State Commun. **77**, 641 (1991).
- ⁴⁰ M.Z. Maialle, E.A. de Andrada e Silva, L.J. Sham, Phys. Rev. B **47**, 15 776 (1993).
- ⁴¹ Supplementary materials present IMX spatial profiles and spectra at different B and P_{ex} , external ring role, bulk emission subtraction, and theory details.
- ⁴² A.L. Ivanov, L.E. Smallwood, A.T. Hammack, Sen Yang, L.V. Butov, A.C. Gossard, Europhys. Lett. **73**, 920 (2006).
- ⁴³ A.T. Hammack, L.V. Butov, J. Wilkes, L. Mouchliadis, E.A. Muljarov, A.L. Ivanov, A.C. Gossard, Phys. Rev. B **80**, 155331 (2009).
- ⁴⁴ Y.Y. Kuznetsova, J.R. Leonard, L.V. Butov, J. Wilkes, E.A. Muljarov, K.L. Campman, A.C. Gossard, Phys. Rev. B **85**, 165452 (2012).
- ⁴⁵ L.V. Butov, L.S. Levitov, A.V. Mintsev, B.D. Simons, A.C. Gossard, D.S. Chemla, Phys. Rev. Lett. **92**, 117404 (2004).
- ⁴⁶ R. Rapaport, G. Chen, D. Snoke, S.H. Simon, L. Pfeiffer, K. West, Y. Liu, S. Denev, Phys. Rev. Lett. **92**, 117405 (2004).
- ⁴⁷ G. Chen, R. Rapaport, S.H. Simon, L. Pfeiffer, K. West, Phys. Rev. B **71**, 041301(R) (2005).
- ⁴⁸ M. Haque, Phys. Rev. E **73**, 066207 (2006).
- ⁴⁹ Sen Yang, L.V. Butov, L.S. Levitov, B.D. Simons, A.C. Gossard, Phys. Rev. B **81**, 115320 (2010).
- ⁵⁰ K. Sivalertporn, L. Mouchliadis, A.L. Ivanov, R. Philp, E.A. Muljarov, Phys. Rev. B **85**, 045207 (2012).